

BigStitcher: Reconstructing high-resolution image datasets of cleared and expanded samples

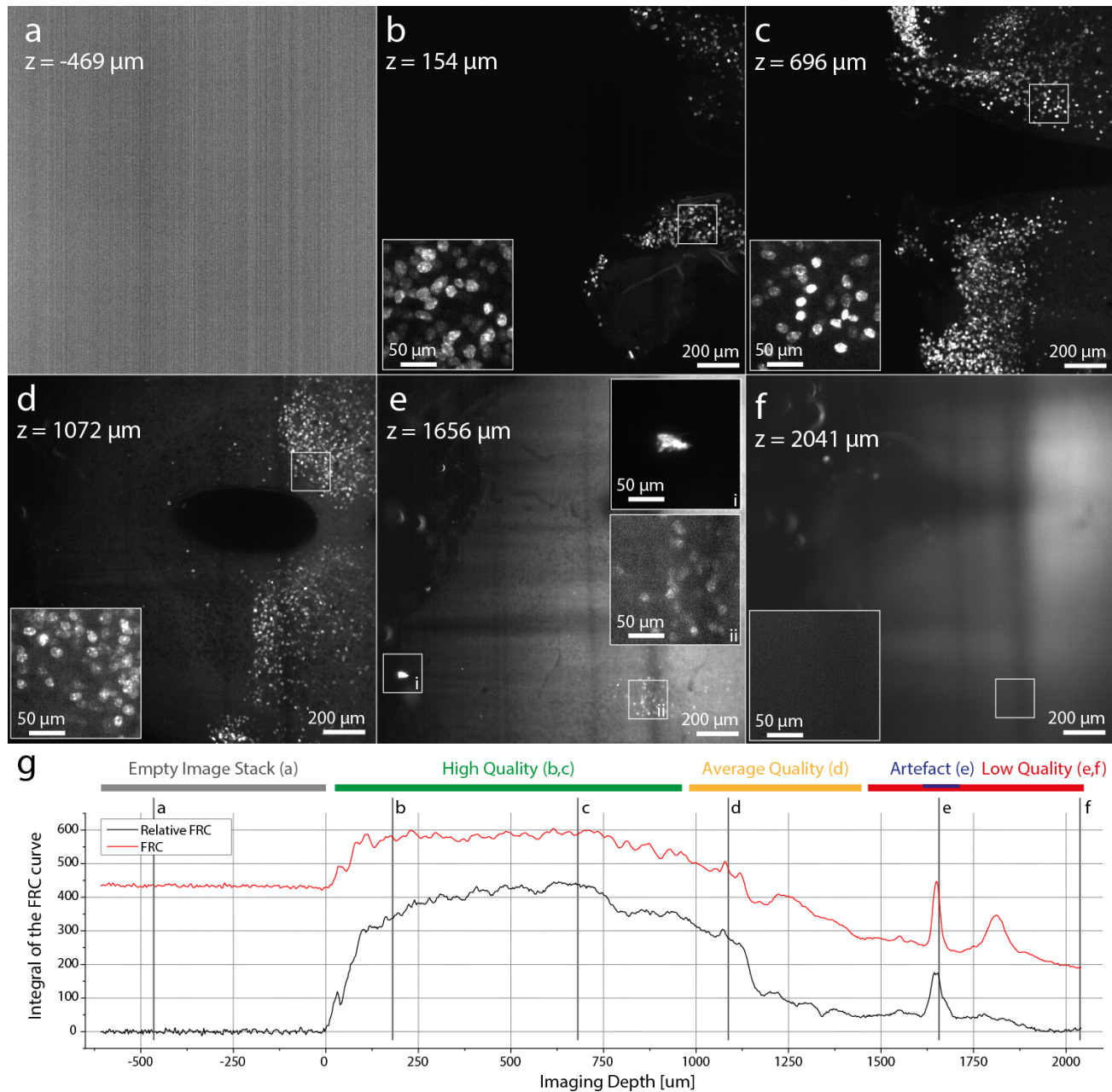
David Hörl[#], Fabio Rojas Rusak[#], Friedrich Preusser, Paul Tillberg, Nadine Randel,
Raghav K. Chhetri, Albert Cardona, Philipp J. Keller, Hartmann Harz, Heinrich Leonhardt,
Mathias Treier, Stephan Preibisch^{*}

Supplementary File	Title
Supplementary Figure 1	Fluorescence preservation in cleared samples
Supplementary Figure 2	Automatic illumination selection
Supplementary Figure 3	Manual alignment
Supplementary Figure 4	Flat-field correction
Supplementary Figure 5	Global optimization
Supplementary Figure 6	Pairwise registration by phase correlation
Supplementary Figure 7	Downsampling with different SNR
Supplementary Figure 8	Downsampling error statistics 1
Supplementary Figure 9	Downsampling error statistics 2
Supplementary Figure 10	Downsampling error statistics 3
Supplementary Figure 11	Interactive inspection and curation of pairwise links
Supplementary Figure 12	Affine refinement via ICP
Supplementary Figure 13	Bounding Box definition
Supplementary Figure 14	Virtual fusion of large image
Supplementary Figure 15	Interest point visualization
Supplementary Figure 16	Manual Transformation of multi-view datasets
Supplementary Figure 17	Expansion Microscopy Stitching
Supplementary Table 1	Datasets used in this publication
Supplementary Note 1-8	Supplementary methods
Supplementary Note 9	BigStitcher User Guide
Supplementary Note 10	Example Datasets for BigStitcher
Supplementary Note 11	Links to the current source codes

Note: Supplementary Videos 1–6 are available for download on the journal homepage.

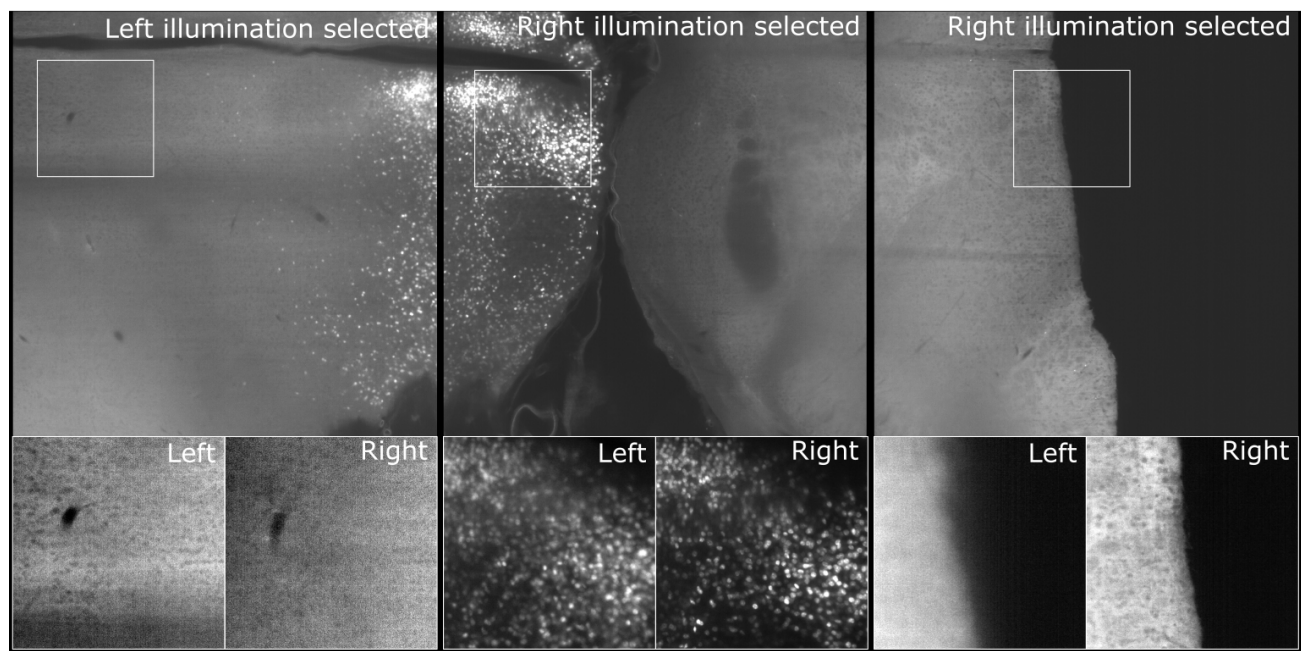
SUPPLEMENTARY FIGURES

SUPPLEMENTARY FIGURE 1: Fluorescence preservation in cleared samples



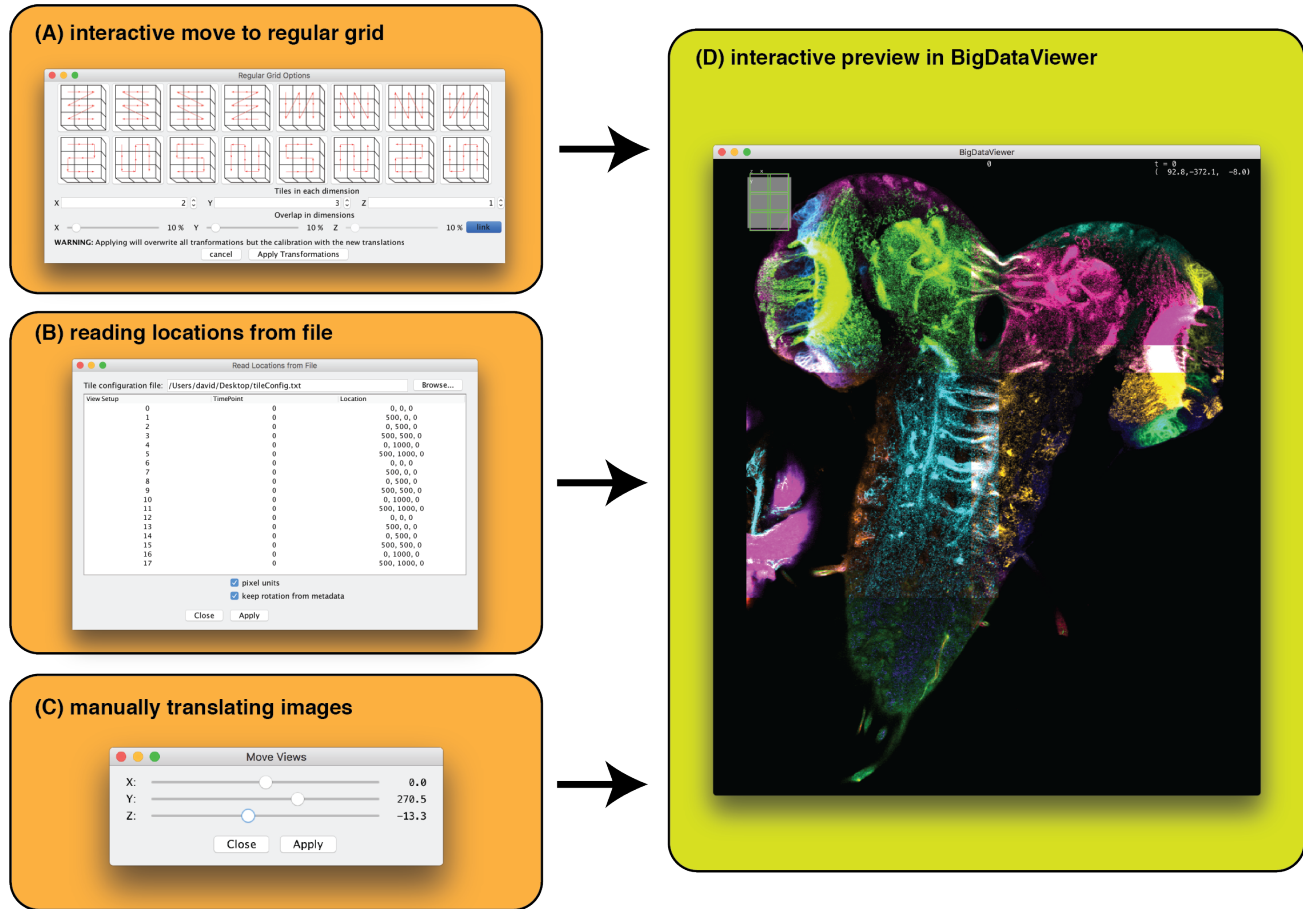
Supplementary Figure 1: *Fluorescence preservation and image analysis in cleared samples.* (a)-(d) Optical sections through an adult mouse hypothalamus in a CLARITY-cleared adult mouse brain expressing H2B-GFP in all bsx neurons. Fluorescence is preserved throughout the clearing procedure. However, the signal is degrading with imaging depth and can typically be recorded up to 1 – 2 cm into the sample, depending on the tissue type and the quality of the clearing process. This maximal imaging depth limits the size of the sample that can be acquired from a single orientation. The brightness and contrast was adjusted individually for each slice. Slight saturation was used to also display the autofluorescent signal.

SUPPLEMENTARY FIGURE 2: Automatic illumination selection



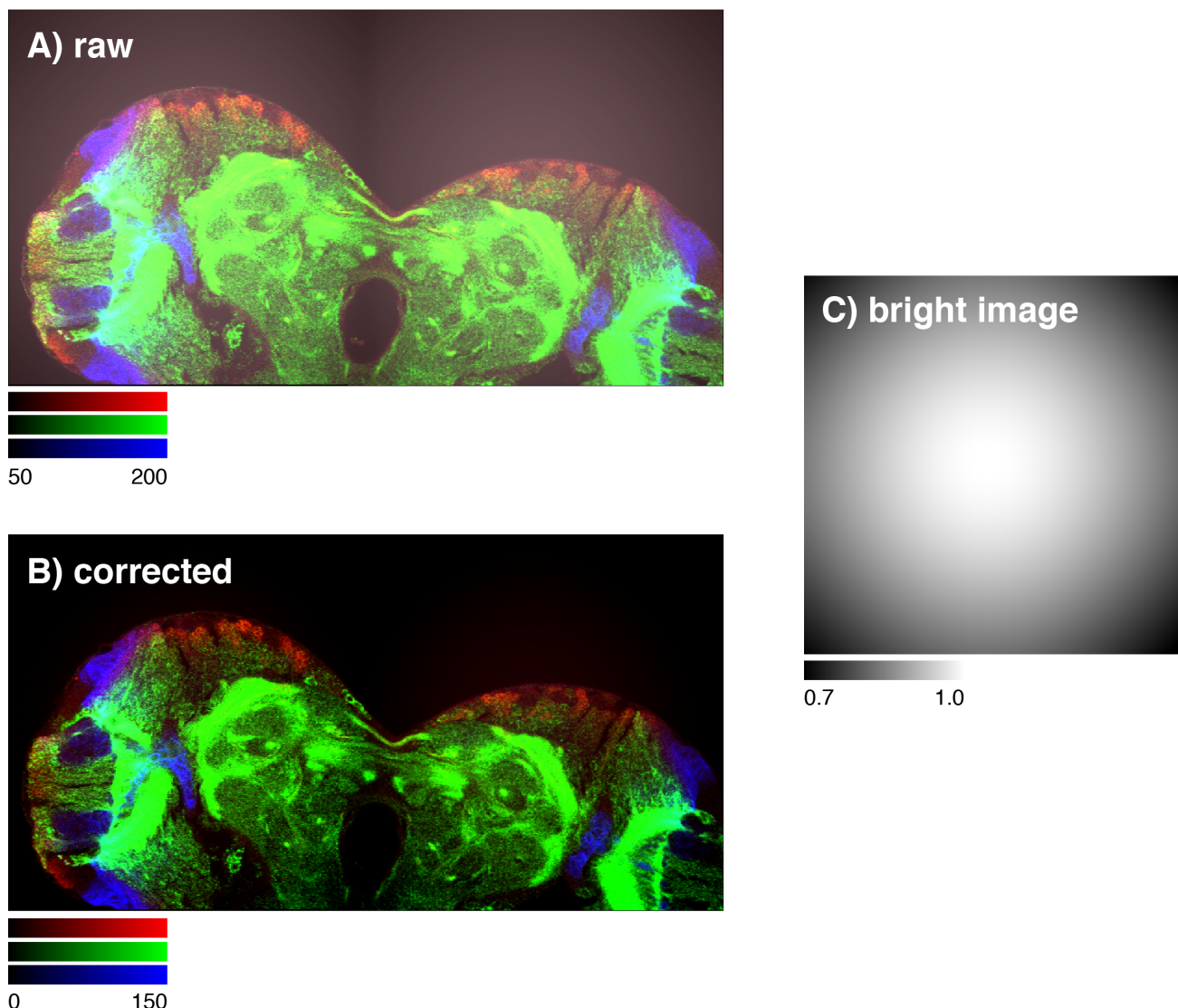
Supplementary Figure 2: *Automatic illumination selection*. Best illumination for three consecutive tiles was selected based on brightest view for each tile. Close-ups shows the specified region for both illumination directions and illustrate that this metric is usually sufficient for a correct decision of the sharper illumination direction of each tile.

SUPPLEMENTARY FIGURE 3: Manual alignment



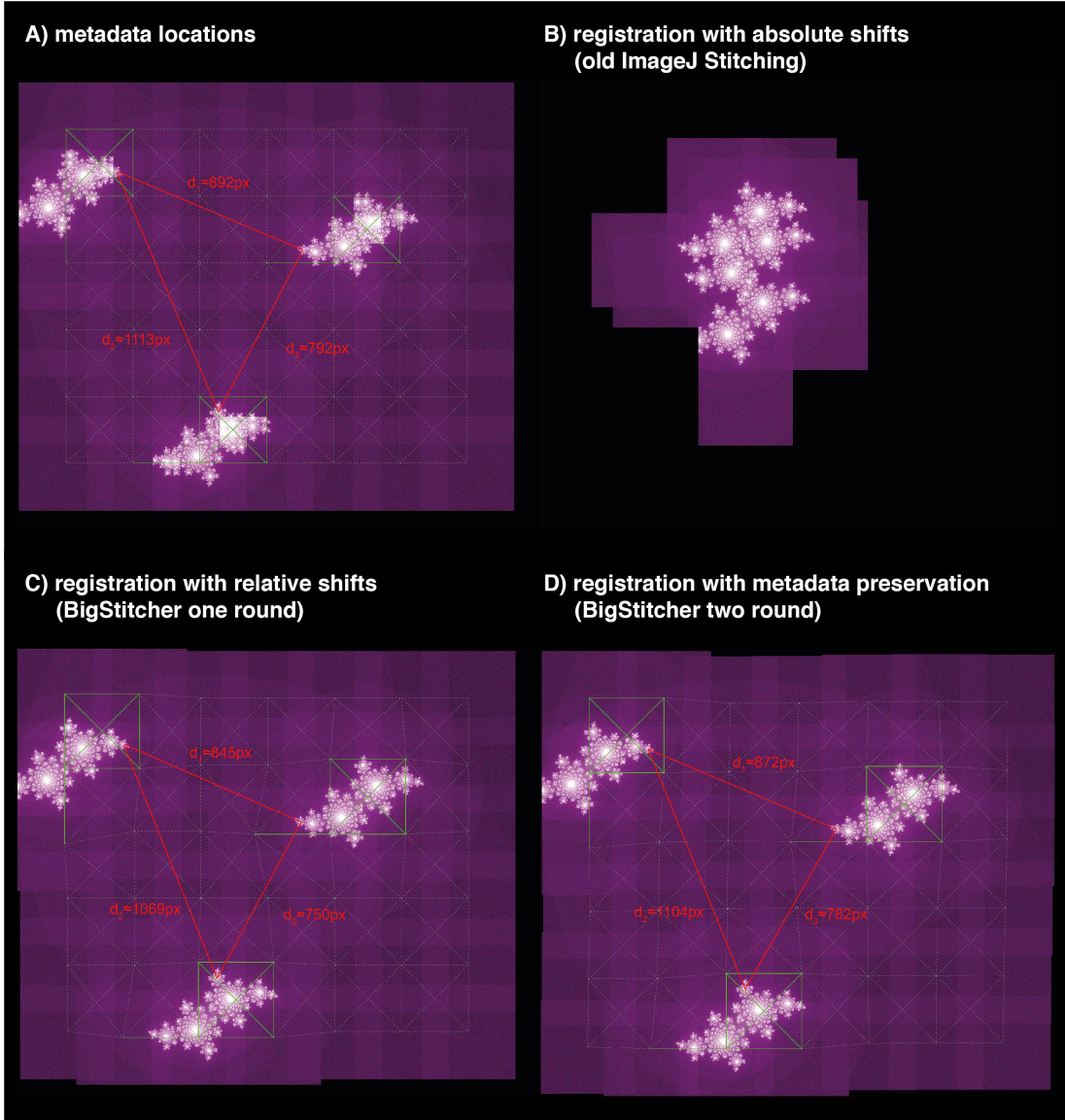
Supplementary Figure 3: *Interactive manual alignment of tiled images.* The BigStitcher GUI offers various ways of manually (pre-)aligning tiled images. **(A)** images can be moved to a regular grid with a given tile order and overlap. **(B)** image locations can also be read from a simple *tile configuration* text file. **(C)** selected image(s) can be moved along axes via sliders. **(D)** all changes will be displayed in the BigDataViewer window immediately **(D)** for quick verification.

SUPPLEMENTARY FIGURE 4: Flat-field correction



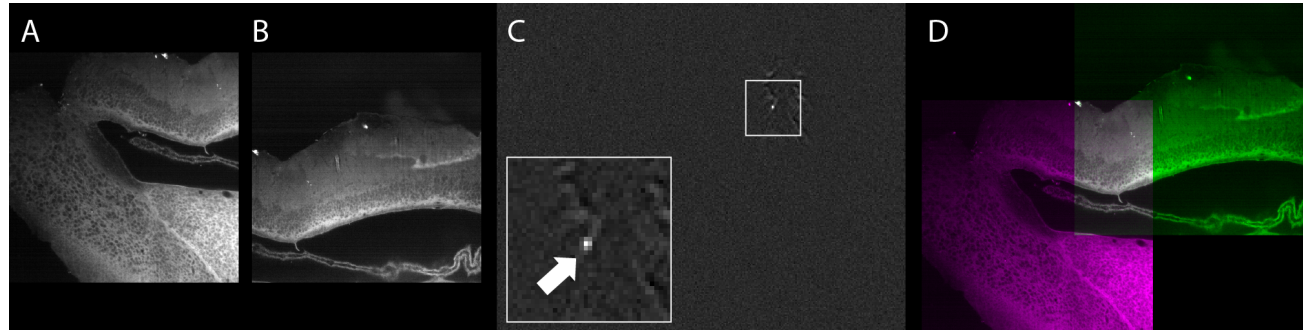
Supplementary Figure 4: *On-the-fly flat-field correction*. The BigStitcher offers correction for camera offsets, fixed pattern noise or uneven illumination. **(A)** Simulation of the effects of a constant background offset and Gaussian illumination/detection efficiency **(C)** on tiled images. By subtracting the *dark image* and modulating with the inverse relative intensity of the *bright image*, such artifacts can be corrected easily **(B)**. The correction is calculated virtually, with optional caching, to allow for immediate inspection of the results.

SUPPLEMENTARY FIGURE 5: Global optimization



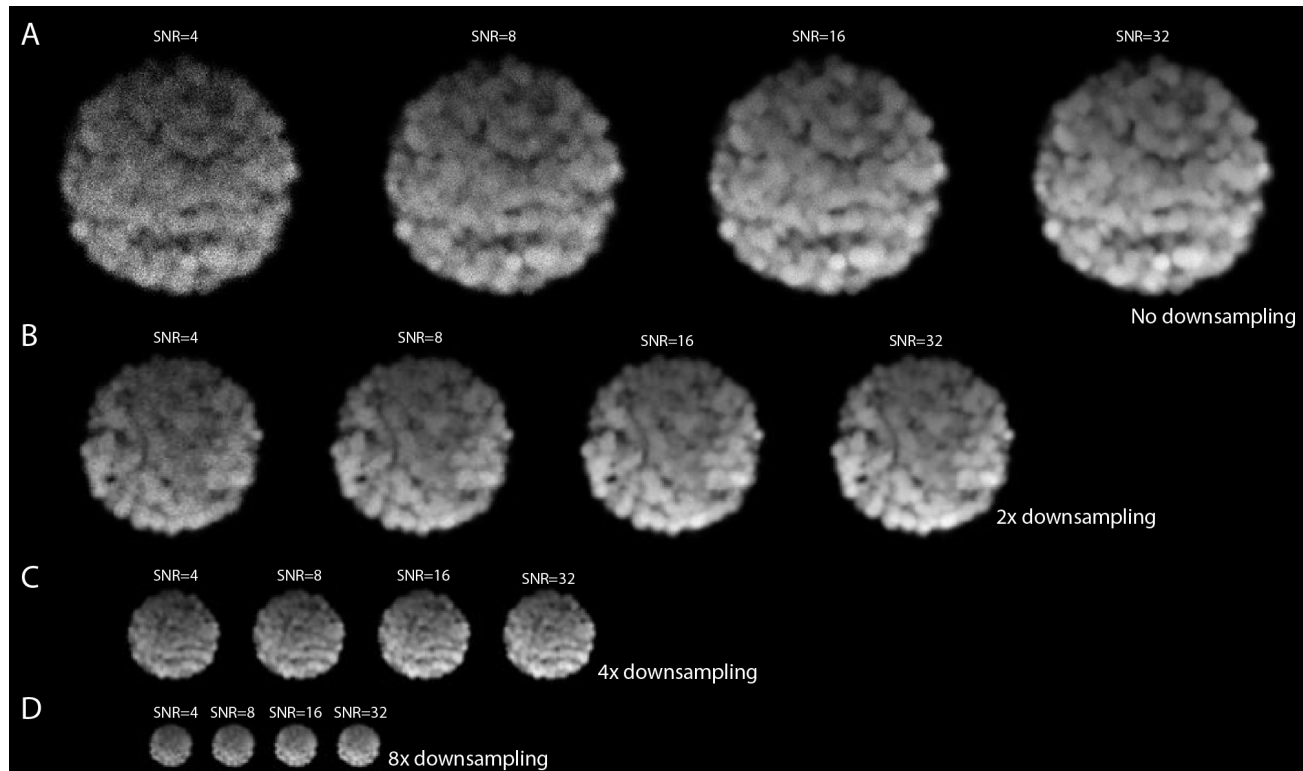
Supplementary Figure 5: *Global optimization of pairwise registration in sparse datasets connected by "empty tiles" (noise only).* **(A)** Simulation of a tiled image dataset with sparse objects: tiled images of multiple translated Julia fractals moved to a grid according to approximate metadata (with too high overlap). Centers of images for which pairwise shifts can be determined via phase correlation are connected by green lines, whereas centers of neighboring tiles for which no meaningful shift can be calculated are linked by dashed grey lines. Manually measured distances between distinct points in the three fractals are shown in red. **(B)** performing global optimization with *absolute shifts* (as it is done BigStitcher's predecessor, the ImageJ Stitching plugin) will correctly align images within connected components of the link graph but place all fractals close to the origin. **(C)** by using *relative shifts*, BigStitcher will leave disconnected objects at their initial location while still aligning within connected components. **(D)** as registrations are not propagated between unconnected tiles, distances between neighboring objects might change. By running a second round of optimization to align connected components according to metadata shifts and applying the results to the in-component registrations, distances between neighboring objects are preserved as-good-as-possible.

SUPPLEMENTARY FIGURE 6: Pairwise registration by phase correlation



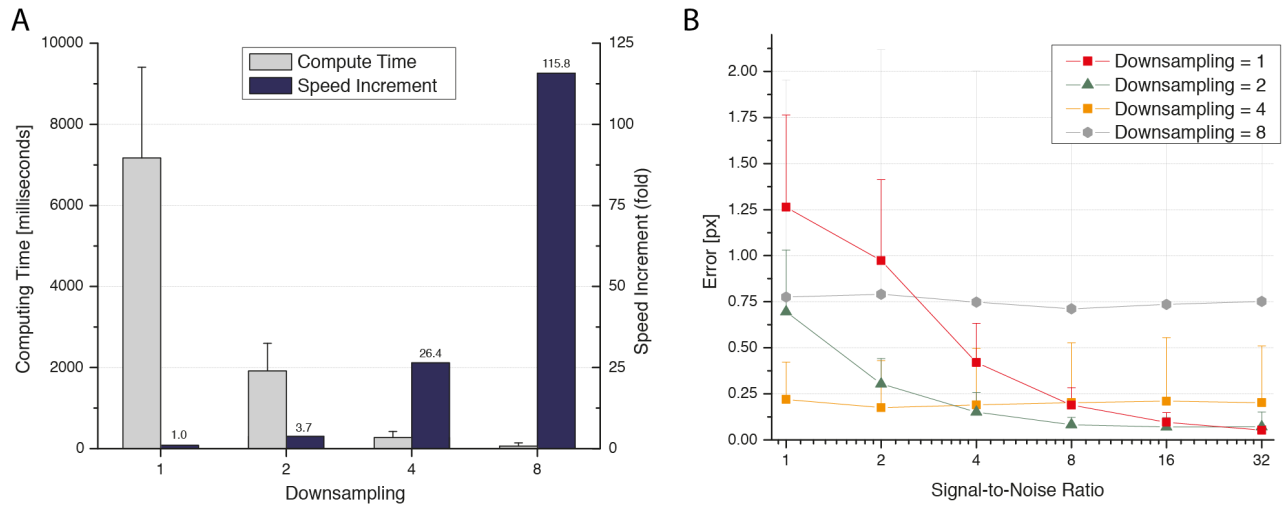
Supplementary Figure 6: *Pairwise registration by phase correlation.* (A),(B) Central slices of image stacks from a tiled acquisition (non-regular tiling) of an adult mouse hypothalamus slice. (C) Phase correlation matrix (PCM) calculated from the two images shows a single, distinct peak above nearly constant background. The peak location corresponds to the relative translation t of both tiles. (D) Central slice through the images aligned according to t , as displayed in interactively during the reconstruction process.

SUPPLEMENTARY FIGURE 7: Downsampling with different SNR



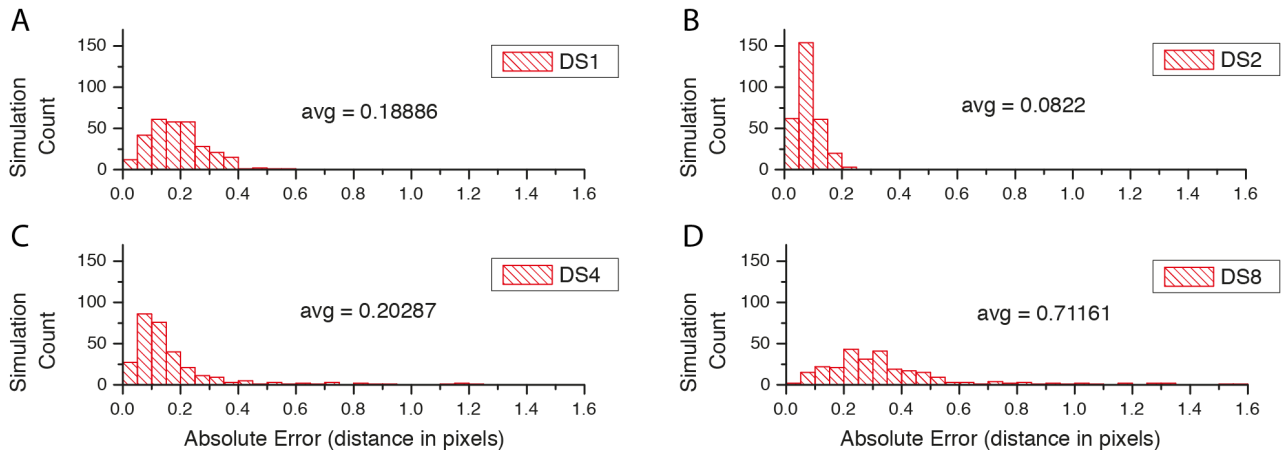
Supplementary Figure 7: *Effects of downsampling on simulated data with different SNR.* (A) Simulated image stacks of spheroid-like objects deteriorated by anisotropic sampling, light attenuation, convolution with an anisotropic PSF, and pixel intensity generation using Poisson processes to archive desired signal-to-noise-ratios (SNRs). A central slice through 3d volumes is shown. (B), (C), (D) Effects of downsampling on the simulated images. The effects of Poisson Shot Noise are gradually reduced by the blurring of increasing downsampling.

SUPPLEMENTARY FIGURE 8: Downsampling statistics 1



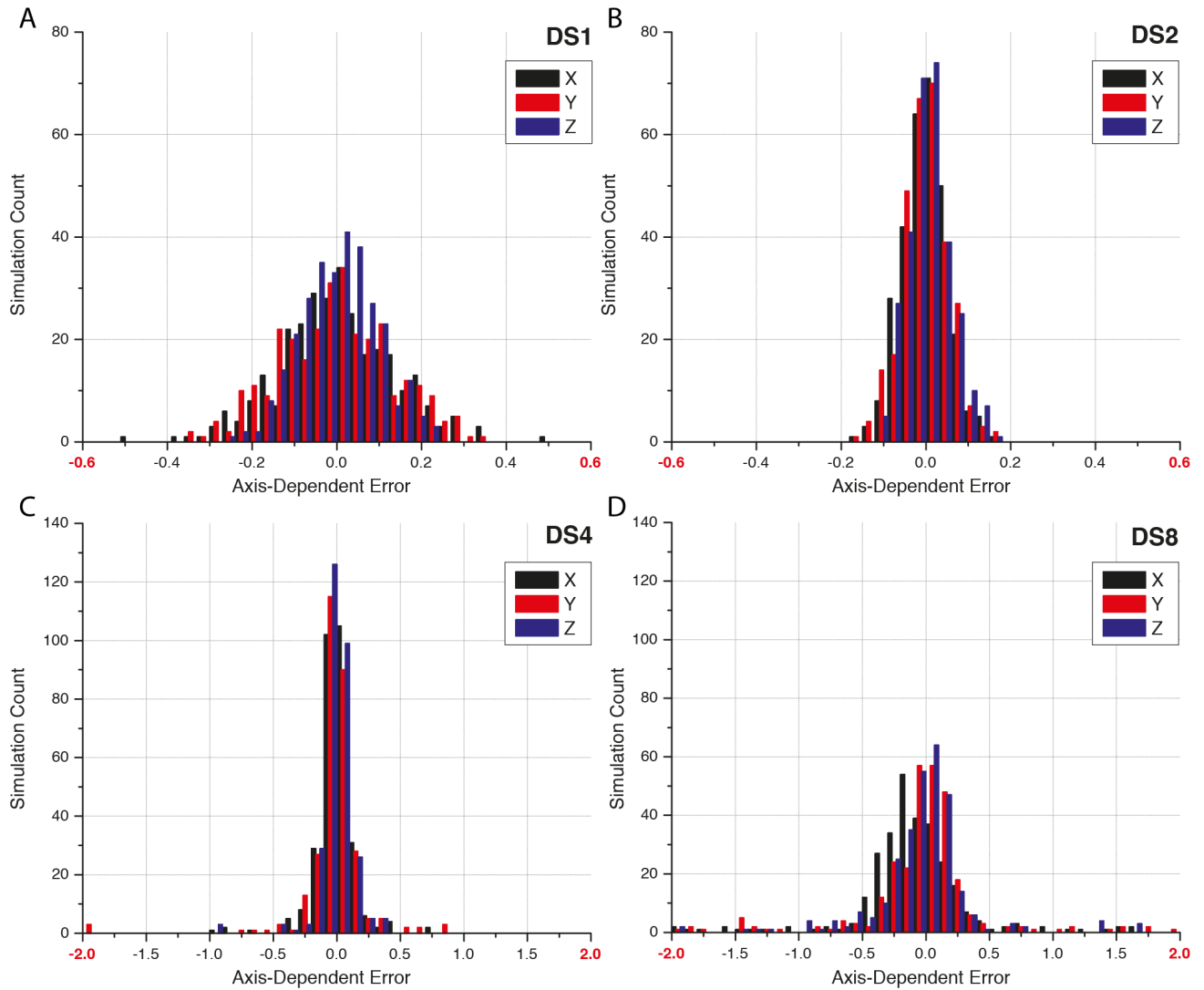
Supplementary Figure 8: *Processing times and overall errors.* **(A)** Processing times for sub-pixel precise identification of overlap between simulation spheroids. With increasing downsampling, the computation time drops significantly. **(B)** Average errors including their standard deviation for all combinations of SNR and downsampling. **(A,B)** All errors are in units of the input images (no downsampling). For each combination of SNR and downsampling 300 independent simulations were run to compute the values.

SUPPLEMENTARY FIGURE 9: Downsampling statistics 2



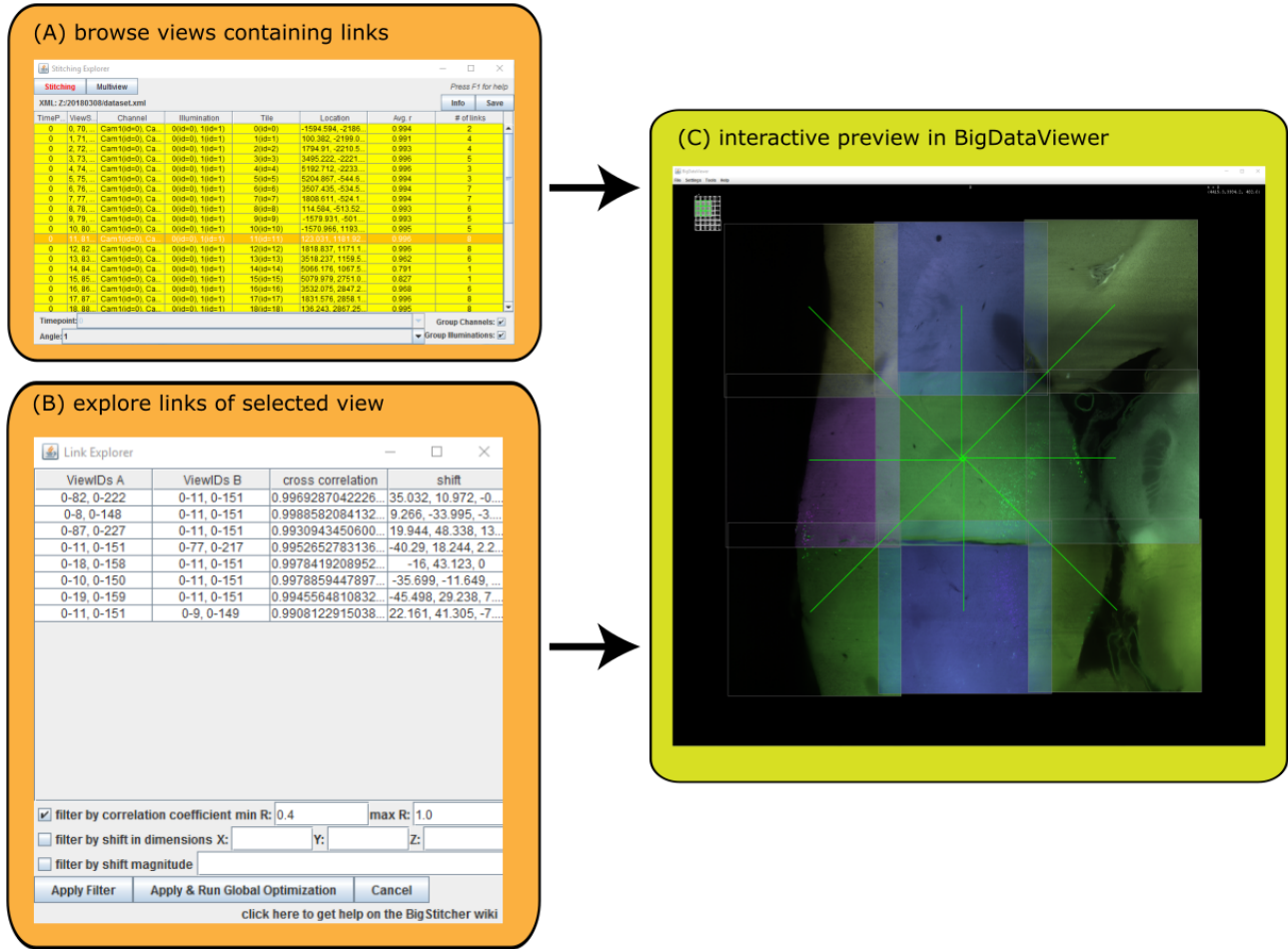
Supplementary Figure 9: *Errors for different downsamplings at SNR=8.* **(A-D)** Histograms showing the distributions of error of the simulations. Errors initially decrease due to the smoothing effect of the downsampling. All errors are in pixel units of the original resolution (DS1). Each histogram consists of 300 independent simulations.

SUPPLEMENTARY FIGURE 10: Downsampling statistics 3



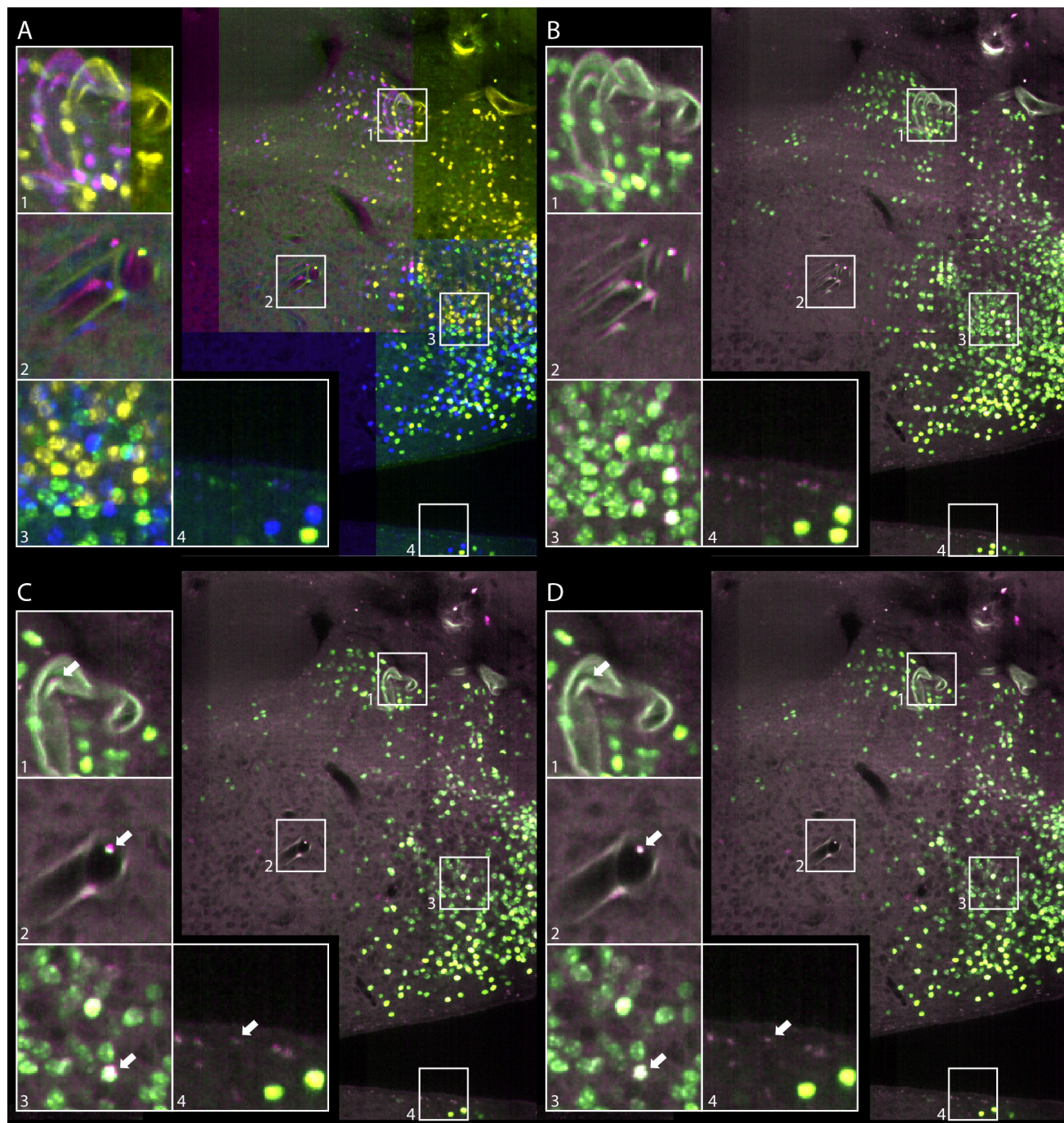
Supplementary Figure 10: *Absolute distance errors at SNR=8.* **(A-D)** Histograms showing the absolute distances between computed and known shift between two simulated spheroids, split by dimension. It illustrates a normal distribution of the error made during the pairwise phase correlation. All errors are in pixel units of the original resolution (DS1). Each histogram consists of 300 independent simulations.

SUPPLEMENTARY FIGURE 11: Interactive inspection and curation of pairwise links



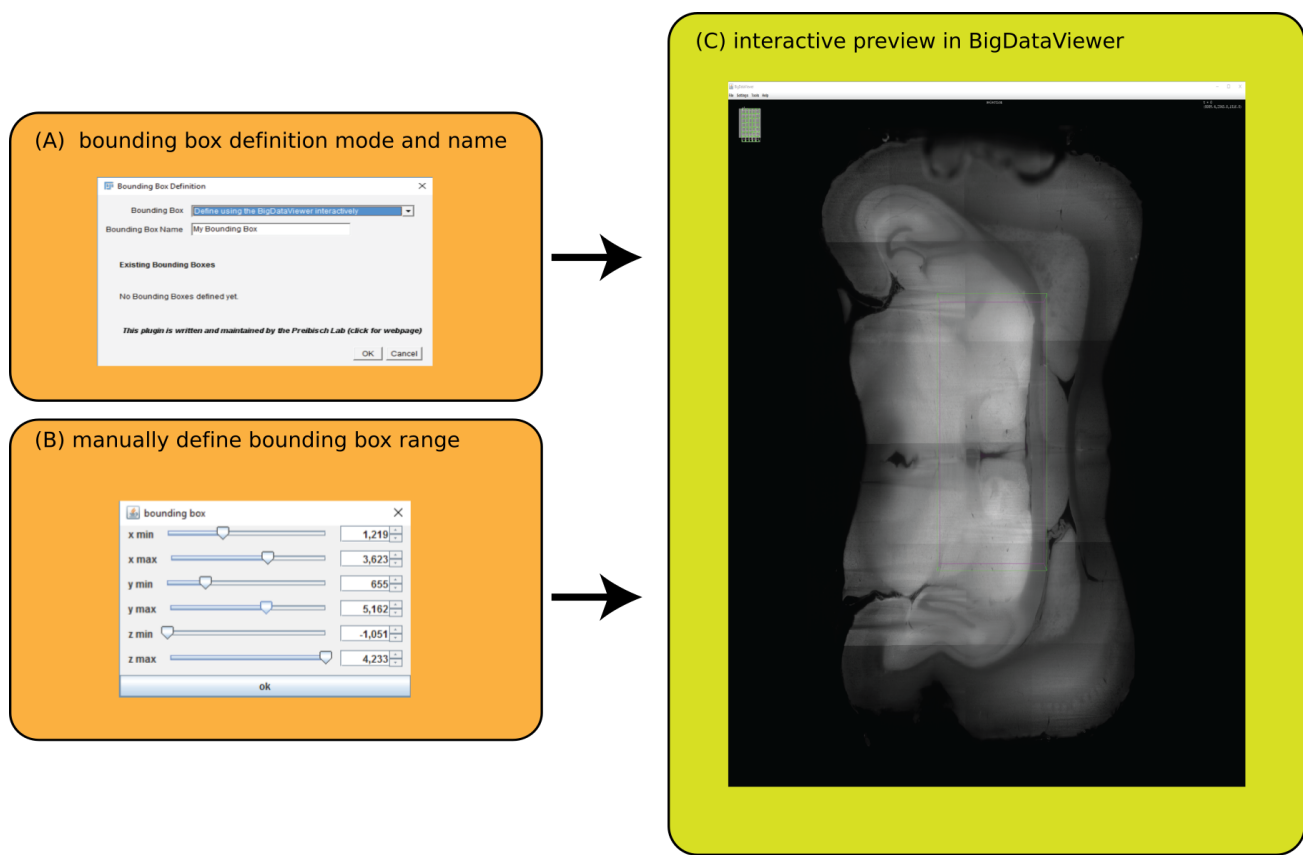
Supplementary Figure 11: *Interactive visualization of links in the link explorer*. The BigStitcher GUI offers to explore and modify calculated links between corresponding tiles in the link explorer menu. **(A)** tiles containing links are displayed in yellow and can be selected. **(B)** display corresponding tiles of the selected view. Single links can be removed manually or through available filtering options. **(C)** corresponding links of the selected view are displayed in real-time in the BigDataViewer.

SUPPLEMENTARY FIGURE 12: Affine refinement via ICP



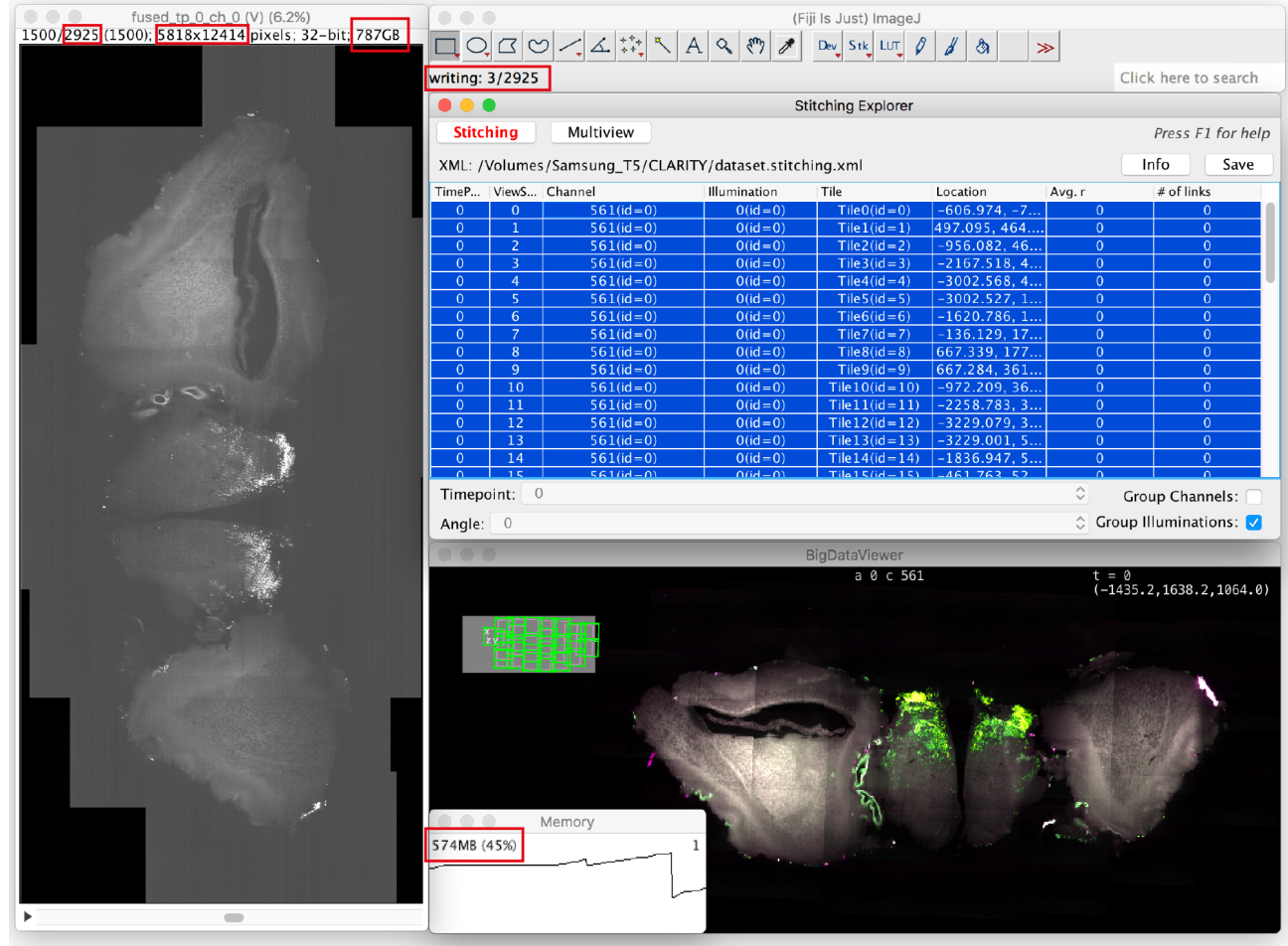
Supplementary Figure 12: *Illustration of different steps for multi-tile alignment* **(A)** Four overlapping image tiles randomly color-coded illustrate the typical error when only the metadata as read from the microscope is applied. **(B)** Shows the same four image tiles as in (A), but without random color coding. **(C)** Quality of the registration after applying the phase-correlation based stitching with downsampling 4 and two-round global optimization. **(D)** Result after applying the automatic ICP refinement for tile alignment and chromatic aberration correction. **(A-D)** Insets highlight specific areas to better appreciate quality differences.

SUPPLEMENTARY FIGURE 13: Bounding Box definition



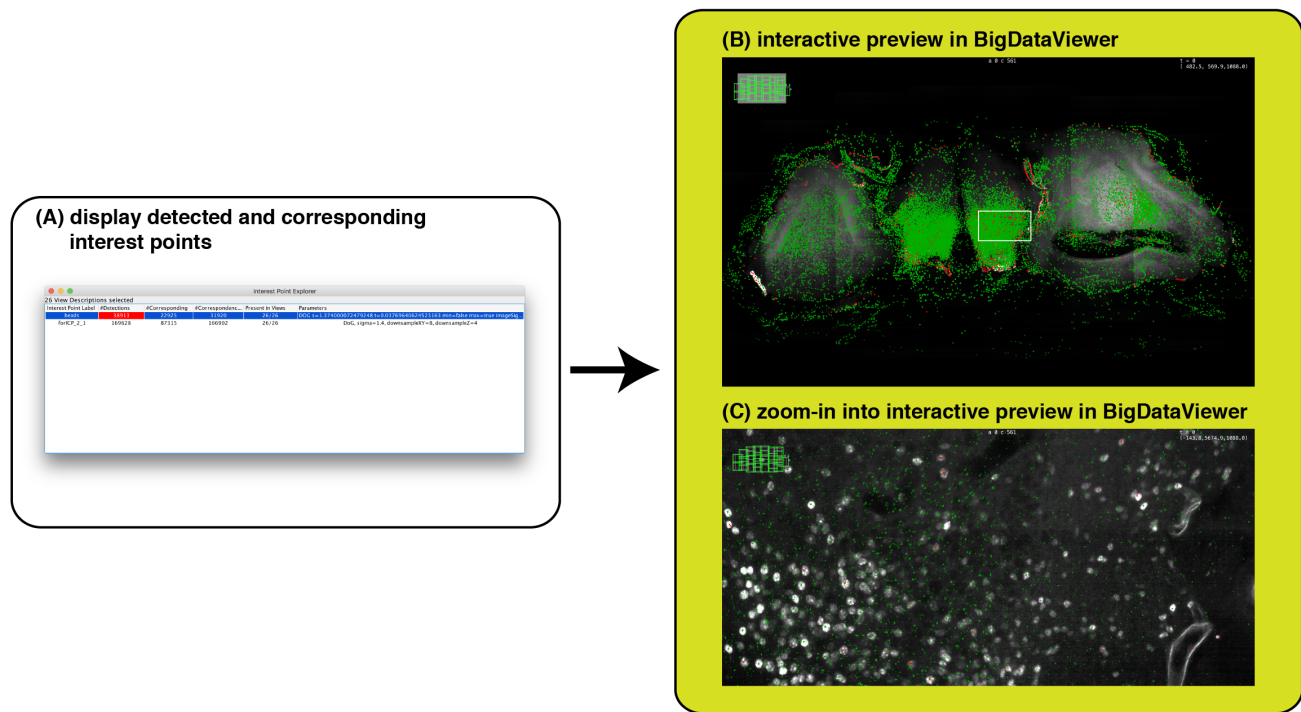
Supplementary Figure 13: *Interactive definition of bounding boxes.* The BigStitcher GUI offers the possibility of defining or modifying regions of interest via the creation of bounding boxes. **(A)** Choose the method used to define a new bounding box. In this case the interactive mode is selected. **(B)** manually define the bounding box range **(C)** Preview the size of the specified bounding box in the BigDataViewer in real-time.

SUPPLEMENTARY FIGURE 14: Virtual Fusion of large image



Supplementary Figure 14: *Virtual Fusion*. Screenshot of a Fiji instance running with **1.25GB of RAM** successfully fusing and saving a **787GB** volume $5818 \times 12414 \times 2925$ pixels in size. This is achieved through **virtual fusion** combined with virtual, cached loading of blocked, multi-resolution input images. Red boxes highlight memory consumption, size, and progress. During the fusion process, the BigStitcher and BigDataViewer are interactively accessible.

SUPPLEMENTARY FIGURE 15: Interest point visualization



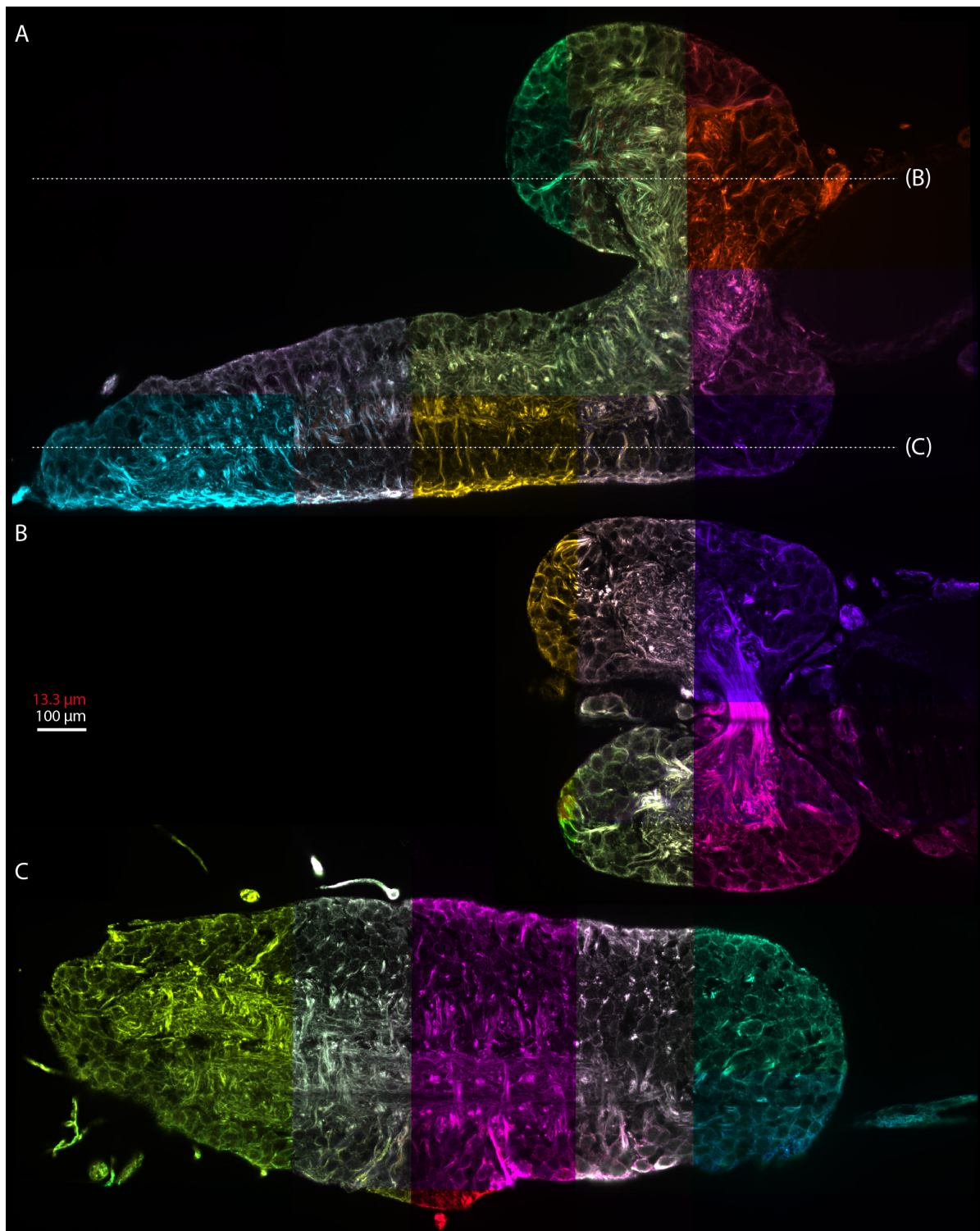
Supplementary Figure 15: *Interactive visualization of interest points.* The interest points explorer allows the visualization of interest points and corresponding interest points between views. **(A)** select desired interest points for visualization. **(B)** preview the interest points overlaid in the BigDataViewer. Red dots intersect with the current image plane, green dots are projections from different z-planes. The white box marks the zoom-in shown in **(C)**. **(C)** Zoom-in into the region outlined in **(B)**.

SUPPLEMENTARY FIGURE 16: Manual Transformation of multi-view datasets



Supplementary Figure 16: *Interactive transformation of views.* Different transformation models can be applied to one or more views and simultaneously visualized in the BigDataViewer. **(A)** Choose transformation model grouping. **(B)** Further define the transformation model. In this case a rotation around the axis is selected. **(C)** Select rotation axis and angle. **(D)** Visualize rotation of the view in the BigDataViewer.

SUPPLEMENTARY FIGURE 17: Expansion Microscopy Stitching



Supplementary Figure 17: *Expansion microscopy stitching* **(A)** All tiles (randomly colored) of one view of the expanded Drosophila central nervous system. Dotted lines highlight orthogonal sections in **(B)** and **(C)**. **(B,C)** Stitching of an orthogonal view showing at two different cut planes. Red scalebar takes expansion into account.

Supplementary Table 1: Summary of all datasets used in this publication.

Dataset	Size	Microscope & Acquisition settings
Coronal slice from a adult mouse brain expressing H2B-eGFP under the neuronal BSX promoter (Figure 2a + Supplement)	1920×1920×1039 16 bit stacks 26 tiles from 1 angles (10% overlap) 2 channels, single illumination 0.36 TB total size	Lightsheet Z.1 with EC Plan-Neofluar 5x/0.16 objective 5.37 μ m LS thickness, 538.3647546 μ m Confocal parameter 0.915×0.915×2.57425409 μ m pixels 119.8ms exposure on PCO.edge camera lasers: 561 nm 100%, 488 nm 80% filters: EF1 BP 505-545, EF 2 BP 575-615
Whole adult mouse brain expressing H2B-eGFP in all BSX-expressing neurons (Figure 1d-n + Figure 2d)	1920×1920×770 16 bit stacks 56 tiles from 2 angles (10% overlap) 2 channels, dual illumination 1.2 TB total size	Lightsheet Z.1 with EC Plan-Neofluar 5x/0.16 objective 5.97 μ m LS thickness, 665.3906758999999 μ m Confocal parameter 0.915×0.915×4.929649351 μ m pixels 119.8ms exposure on PCO.edge camera lasers: 561 nm 40%, 488 nm 40% filters: EF1 BP 505-545, EF 2 BP 575-615
Coronal slice through an adult mouse brain expressing an H2B-eGFP lineage tracing marker in BSX-expressing neurons (Figure 2b + Supplement)	1920×1920×645 16 bit stacks 63 tiles from 2 angles (10% overlap) 2 channels, dual illumination 1.1 TB total size	Lightsheet Z.1 with EC Plan-Neofluar 5x/0.16 objective 10.44 μ m LS thickness, 2034.834282 μ m Confocal parameter 0.915×0.915×6.203581395 μ m pixels 119.8ms exposure on PCO.edge camera lasers: 561 nm 40%, 488 nm 40% filters: EF1 BP 505-545, EF 2 BP 575-615
	1920×1920×828 16 bit stacks 35 tiles from 2 angles (10% overlap) 2 channels, dual illumination 0.78 TB total size	Lightsheet Z.1 with EC Plan-Neofluar 5x/0.16 objective 10.44 μ m LS thickness, 2034.834282 μ m Confocal parameter 0.915×0.915×4.930096618 μ m pixels 119.8ms exposure on PCO.edge camera lasers: 561 nm 50%, 488 nm 50% filters: EF1 BP 505-545, EF 2 BP 575-615
	1920×1920×960 16 bit stacks 35 tiles from 2 angles (10% overlap) 2 channels, dual illumination 0.9 TB total size	Lightsheet Z.1 with EC Plan-Neofluar 5x/0.16 objective 10.44 μ m LS thickness, 2034.834282 μ m Confocal parameter 0.915×0.915×4.930916667 μ m pixels 119.8ms exposure on PCO.edge camera lasers: 561 nm 50%, 488 nm 50% filters: EF1 BP 505-545, EF 2 BP 575-615

Continued on next page

Supplementary Table 1: Summary of all datasets used in this publication.

Dataset	Size	Microscope & Acquisition settings
Whole <i>C. elegans</i> during dauer with all neuron nuclei expressing tagRFP in and co-stained with DAPI(Figure 2f)	750×1920×40 16 bit stacks 16 tiles from 4 angles (10% overlap) 2 channels, single illumination 0.003 (2.96GB) TB total size	Lightsheet Z.1 with W Plan-Apochromat 20x/1.0 objective (2× zoom) 1.82 μ m LS thickness, 56.72238239 μ m Confocal parameter 0.114×0.114×0.8035 μ m pixels 59.9ms exposure on PCO.edge camera lasers: DAPI 505 nm 2%, DAPI 561 nm 0.2%, RFP 561 nm 5% filters: DAPI CAM BS Mirror, RFP CAM BS SBS LP 560, RFP EF 1 BP 575-615
Central nervous system of a Drosophila 1st instar larva with immunostaining for tubulin(Figure 2c,e + Supplement)	2048×2048×923 stacks ? tiles from 4 angles (28% overlap) 1 channels, dual illumination ? TB total size	IsoView with SpecialOptics 16x/NA 0.71 objective 4.92 μ m LS thickness, 416.0 μ m Confocal parameter 0.4125×0.4125×0.8125 μ m pixels ?ms exposure on Orca Flash 4.0 v2 sCMOS camera lasers: 488 nm Laser? filters: ?

SUPPLEMENTARY NOTES

1. Data Import

SpimData data format

We internally represent our image data and metadata using an extended version of the SpimData data format of BigDataViewer.² Each image stack is defined by a (ViewSetup, TimePoint)-combination. We extend the format by giving each ViewSetup the following *attributes*: Channel to represent color channels, Illumination to represent illumination directions, Angle to represent multi-view acquisition angles and finally Tile, representing (local) x,y points in a multipoint acquisition.

In addition to those attributes, we store detected interest points, bounding boxes (named sub-volumes in which we can *fuse* or deconvolve images), point spread functions for deconvolution and pairwise registrations (that have yet to be used in global optimization) for each (ViewSetup, TimePoint) *view*. For each image stack, we also store its *registration* (i.e. the transformation from pixel to world coordinates) as a list of affine transform matrices. The registration steps described below will typically prepend another transformation matrix to this list. Finally, the SpimData is associated with an ImgLoader object that can make image pixel data available as an ImgLib2³ RandomAccessibleInterval given a (ViewSetup, TimePoint) *view id*.

The SpimData data structure can be saved as an XML *project file*, allowing users to manually edit it with any text editor. We automatically save previous versions of the project file to provide the user with the ability to un-do registration steps.

Import of data

BigStitcher imposes little constraints on the format and naming of raw data files. Using the Bioformats⁴ library, we support a large variety of image file formats, from "conventional" TIFF stacks to vendor-specific formats. The assignment of attributes to the image stacks in the raw data can be done automatically or with minimal interaction from the users. We offer the possibility to immediately compute multi-resolution pyramids from the images and saving them as chunks to HDF5 files. Furthermore, making use of cached ImgLib2 data structures, we support virtual loading of image planes from the raw files with caching of already loaded planes.

2. Flat-field correction

Flat-field correction is the process of correcting for image artifacts due to uneven illumination or detection efficiency or fixed-pattern noise. Aside from being visually unpleasing, especially in tiled acquisitions, these artifacts can also effect image registration and downstream quantitative image analyses. We therefore offer simple on-the-fly correction for a *dark image* (which might be nonzero due to e.g. camera offset) and a *bright image* (representing uneven illumination or detection efficiency across the field-of-view). We calculate corrected pixel intensities C from a raw image R and bright and dark images B and D as:

$$C_x = \frac{(R_x - D_{x'}) * \overline{(B - D)}}{(B_{x'} - D_{x'})} \quad (1)$$

The correction images can either have the same dimensionality as the raw images, in which case $x' = x$, or have lower dimensionality (e.g. when using 2D correction images on a 3D image stack), in which case $x' = (x_1 \dots x_n)$ with n being the dimensionality of the correction images. If a dark image is not provided by the user, we assume it to have constant intensity of 0 (corresponding to no background offset). Likewise, if no bright image is provided, we assume it to have constant intensity of 1 (uniform illumination and detection efficiency).

We implemented the flat-field correction as a wrapper around an ImgLoader, calculating corrected pixel intensity values on-the-fly (with optional caching) every time an image is loaded. That way, the corrected

images are available for all other processing steps such as intensity-based registration, interest point detection or image fusion, but it is still possible to activate or de-activate the correction or change bright or dark images after the initial flat-field correction. A separate (bright, dark)-correction image pair can be set for every image in the dataset by modifying the XML project file, while in the GUI we offer user-friendly assignment of correction images to every (channel, illumination direction)-pair.

3. Pairwise shift calculation

In BigStitcher, we currently offer three ways of calculating shifts between a pair of images: the Fourier-based *phase correlation* algorithm, the Gradient-descent-based *Lucas-Kanade* algorithm, both intensity-based methods, as well as interest point-based alignment.

Phase correlation

By default, we calculate pairwise translational shifts of two images I_1 and I_2 using phase correlation^{5,6} as explained in the **Online Methods** section.

Lucas-Kanade

In addition to the default phase correlation-based pairwise shift calculation, we offer registration via an ImgLib2 implementation of the *inverse compositional* formulation of the gradient descent-based Lucas-Kanade optical flow algorithm.⁷ While the algorithm is applicable to a variety of transformation models, we currently stick to estimating a translation vector t . If the pairwise registration converges, we calculate the cross correlation of the overlapping portions of the images as a quality metric for the pairwise registration.

Intensity-based Registration of grouped images

In many use cases, one might want to align not single images but groups of images, e.g. all channels of a tile, in the pairwise registration step. For this, we implemented a flexible framework for the registration of grouped images.

Each attribute of the images can be set to be an *axis of application*, an *axis of comparison* or an *axis of grouping*. The registration will proceed by first splitting the images by the application attributes, i.e. grouping all images that have the same value for these attributes. In each group, the images are then split by the comparison attributes and finally, the remaining image groups (that differ only in the grouping attributes) are combined into one image stack by either averaging all images for each grouping attribute or picking the image with a specific instance of the attribute.

In a typical application, the stitching of tiled datasets, we would, for example, start by *applying* the registration to all (Angle, TimePoint)-combinations individually, *comparing* by Tiles and finally *grouping* by Illumination and Channel for each tile, e.g. by averaging illumination directions and picking a specific channel.

Intensity-based registration of images with pre-registrations

The two images I_1 and I_2 can have arbitrary pre-registrations, i.e. pixel coordinates x_{px} are mapped to world coordinates x_w via the affine transforms $x_{w,I_1} = A_{I_1}x_{px,I_1} + b_{I_1}$ and $x_{w,I_2} = A_{I_2}x_{px,I_2} + b_{I_2}$. Depending on the values of A_{I_1} and A_{I_2} , we consider two cases: If they are equal, i.e. the pre-registrations differ only by a translation, we perform the shift calculation on the raw pixel data of the overlapping volume to get a shift vector t for I_2 in pixel coordinates. The transformation in world coordinates is then given by $R \begin{pmatrix} I & t \\ 0 & 1 \end{pmatrix} R^{-1}$ with $R = \begin{pmatrix} A_{I_2} & b_{I_2} \\ 0 & 1 \end{pmatrix}$. If the pre-registrations differ in more than just translation, we create virtually transformed images of the smallest rectangular bounding box enclosing the overlapping volume and use them as input to the registration. As the virtual input images are already in world coordinates in this case, the resulting transformation matrix for I_2 is simply $\begin{pmatrix} I & t \\ 0 & 1 \end{pmatrix}$.

Interest-point based

For interest-point based pairwise registration, we detect local extrema in either Difference-of-Gaussian or Difference-of-mean filtered images, optionally followed by subpixel refinement of the detections via a quadratic fit.⁸ If we are registering a pair of image *groups*, the interest points of each image in the group are pooled, with optional replacement of point clusters within a user-defined radius by their center.

For each image, we apply the current (affine) registrations to the pixel-coordinate interest points and then determine *candidate point matches* via descriptor matching.^{9,10} We then perform model-based outlier removal via the RANSAC algorithm,¹¹ yielding a set of *inlier point pairs*, $C_{inliers}$, and an optimal translation t for I_2 , minimizing $\sum_{(ip_1, ip_2) \in C_{inliers}} \|ip_1 - ip_2 - t\|^2$

4. Global optimization

Estimation of globally optimal transformations

The pairwise registration step results in *links* between image (groups) V (note that since we do not use the actual image *content* in the global optimization, we will refer to the images by their integer *id* in this section: $V \subset \mathbb{N}$). The links can be either in the form of pairwise transformations T^p (such that coordinates x from two images V_i and V_j can be transformed according to $T_{ij}^p(x_j) = x_i$) or *point correspondences* PM from which such transformations can be estimated. The pairwise registrations thus form a *link graph* (V, C) with edges $C = \{(i, j) \in V \times V | T_{ij}^p \in T^p\}$ between image pairs for which we could determine pairwise transformations. Simply traversing a spanning tree of the link graph and propagating the pairwise transformations can lead to the compounding of pairwise registration errors, even if the traversal is done along a *minimal* spanning tree determined according to some quality metric q_{ij} , e.g. cross-correlation, of the pairwise registrations.

We thus make use of an algorithm for globally optimal registration by iterative minimization of square displacement of point correspondences^{12,13} for reaching a reasonable consensus in this case. This point match-based framework allows for flexible grouping and fixing of images, is applicable to, among others, time series-, chromatic channel- or view-registration and can easily be adapted to incorporate the pairwise transformations from e.g. phase correlation. The algorithm is agnostic of the transformation model (e.g. translation, affine transform,...), with the only requirement being that the model parameters can be estimated by a least-squares fit from point correspondences.

We determine the globally optimal registrations R given the image (groups) V , pairwise links C , pairwise n -dimensional point matches PM with $PM_{ij} \subset \mathbb{R}^n \times \mathbb{R}^n$ and a set of fixed views $F \subseteq V$ by minimizing:

$$\arg \min_{R \setminus \{R_i | V_i \in F\}} \sum_{(i, j) \in C} \left(\sum_{(x_k, y_k) \in PM_{ij}} \|R_i(x_k) - R_j(y_k)\|^2 \right) \quad (2)$$

Note that for all fixed views, the registration will be constrained to be the identity transformation I : $\forall V_i \in F : R_i = I$.

Global optimization given pairwise transformations

The intensity-based pairwise shift calculations do not directly give us the point correspondences we need for the global optimization step, instead the results are pairwise transformations T^p in the form of affine transform matrices. We can, however, easily construct point correspondences by taking a set of points and transforming them with the *inverse* transform (the only requirement being that the n -dimensional points do not all lie in a subspace of lower dimensionality of \mathbb{R}^n).

Using the 3-dimensional pairwise transformations T^p ($T_{ij}^p(x_j) = x_i$) between two image (groups) V_i and V_j given their existing registrations R^{meta} , we use the 8-point approximate bounding box of their overlapping region BB_{ij} to construct the point correspondences: $PM_{ij} = \{(bb_k, (T_{ij}^p)^{-1}(bb_k)) | bb_k \in BB_{ij}\}$. We can then determine the globally optimal registrations R by performing the minimization described above (2).

Global optimization with iterative link dropping

Once the global optimization terminates due to convergence or exceeding of the maximum number of iterations, we can calculate the *error* of the individual images as the average displacement of all interest points in an image to their point matches:

$$e_i = \frac{\sum_{\{j:(i,j) \in C\}} \sum_{(x_k, y_k) \in PM_{ij}} \|R_i(x_k) - R_j(y_k)\|}{\sum_{\{j:(i,j) \in C\}} |PM_{ij}|} \quad (3)$$

If the link graph (V, C^n) contains links with contradicting point correspondences, stopping after one round of global optimization might leave us with unsatisfying results. In the *iterative* version of the global optimization, we therefore check that both the average error of all images and the ratio of maximal and average error fall below a user-defined threshold. If these conditions are not yet met, we will proceed to iteratively remove disagreeing links from the link graph and repeat the global optimization. To do this, we first determine the link with the highest error by maximizing:

$$c_{worst} = \arg \max_{(i,j)} \max_{(x_k, y_k) \in PM_{ij}} \left((1 - q_{ij})^2 \sqrt{d_{ijk}} \log_{10} \left(\max(\deg(i), \deg(j)) \right) \right) \quad (4)$$

with d_{ijk} denoting the distance of the k 'th point match of the link (i, j) , $d_{ijk} = \|R_i(x_k) - R_j(y_k)\|$, $\deg(i)$ denoting the degree (number of neighbors) of an image V_i in the link graph and q_{ij} being a *quality metric* $\in (0, 1)$ of the link, e.g. 0-truncated cross correlation. We then remove the worst link from the links ($C^{n+1} \leftarrow C^n \setminus c_{worst}$) and repeat the optimization step 2 with the new link graph (V, C^{n+1}) . The whole process is repeated until the errors fall below a user-defined threshold (in the worst case, links will be dropped until we end up with *spanning trees* of the connected components in the link graph).

Two-round global optimization using metadata

If some cases, the link graph might contain multiple connected components, e.g. in datasets from screening applications, where the actual sample only occupies isolated "islands" and most images contain only background. In this case, we can only reliably determine pairwise transformations within the connected components and align images within the components in the global optimization step. We might, however, have reasonable registrations R^{meta} from metadata and wish to keep as closely as possible to those if we do not have *strong* links.

For this, we developed a *two-round* version of the global optimization. In the first round, we determine registrations R^{strong} as described above, using the graph of *strong* links, i.e. links that are backed by pairwise transformations. In the second round, we determine the connected components in the (V, C^{strong}) graph and a mapping $CC : \mathbb{N} \rightarrow \mathbb{N}$ from image (group) indices to connected component indices as well as *weak links* $C^{weak} = \{(i, j) \in V \times V | CC(i) \neq CC(j)\}$ between images in different components. We then determine transformations R^{cc} for each connected component not containing a fixed image by minimizing:

$$\arg \min_{R^{cc} \setminus \{r_i^{cc} \in R^{cc} | CC_i \cap F \neq \emptyset\}} \sum_{(i,j) \in C^{weak}} \sum_{bb_k \in BB_{ij}} \|R_{CC(i)}^{cc}(R_i^{strong}(bb_k)) - R_{CC(j)}^{cc}(R_j^{strong}(bb_k))\|^2 \quad (5)$$

Note that we use the corners bb_k of the bounding box BB_{ij} of the overlapping volume of two images V_i and V_j as the point correspondences. The overlap is determined according to the metadata transformations R^{meta} and we essentially try to "un-do" the registrations of the first round as well as possible (while keeping the registrations *within* the connected components). The final transformations R are the concatenation of the registrations within the connected components with the relative transformations of the connected components: $R_i \leftarrow R_{CC(i)}^{cc} R_i^{strong}$.

5. MultiView Registration

For MultiView registration, e.g. registration of angles or time series stabilization, we first detect interest points in the individual images as described above (3). Images may be grouped (and are by default if we are, e.g. registering tiled acquisitions from multiple angles for which we already aligned the tiles via an intensity-based method) according to their attributes, by pooling their interest points and optionally merging clusters.

Pairwise point correspondences can either be established by descriptor matching followed by RANSAC outlier removal, a modified version of the iterative closest point (ICP) algorithm or by simply matching the center of mass of the point clouds of both images (note that in this case the registration will be constrained to be a translation). Using the link graph (V, C) and pairwise point correspondences P_{ij} established thus, we calculate the final registration by performing global optimization as described above (4), optionally with iterative link removal and a second round to preserve metadata.

6. Image Fusion

We *fuse* multiple images by performing a weighted average of the raw images I^{raw} transformed by their registrations R . Each raw image I_i^{raw} has a set weight images W_i . For example, we allow the user to weigh the images with a cosine-shaped fade-out, de-emphasizing the artifact-prone border regions of the individual images, as well as by the approximate local entropy, to emphasize images with sharper structures in overlapping regions. Since the raw images will be evaluated at non-integer coordinates, we offer the choice between nearest-neighbor and linear interpolation. Downsampling can easily be achieved by prepending a scaling transformation to each of the registrations R . The intensity of the fused volume at a coordinate x is given by:

$$I^{fused}(x) = \frac{\sum_{I_i^{raw} \in I^{raw}} \left(I_i^{raw}(R_i^{-1}(x)) * \prod_{w_j \in W_i} w_j(R_i^{-1}(x)) \right)}{\sum_{I_i^{raw} \in I^{raw}} \left(\prod_{w_j \in W_i} w_j(R_i^{-1}(x)) \right)} \quad (6)$$

In practice, we evaluate I^{fused} only at integer coordinates of a user-defined *bounding box*. We implemented the image fusion to perform all calculations virtually on-the-fly, with caching of previously computed planes using imglib2-cache. This allows the quick inspection of fusion results as well as creation and planewise saving of images that might exceed the RAM available to the user.

7. Brightness and Contrast adjustment

Even after correcting for fixed-pattern noise (2), differences in brightness and contrast between images, e.g. due to bleaching, might persist and be visible in the fused images. To correct for this, we estimate optimal linear transforms of pixel intensities in adjacent images¹⁴ to achieve uniform brightness and contrast in the whole dataset. We minimize the intensity difference of all pixels in the overlapping volume O_{AB} of two images I_A, I_B (with corresponding coordinates (x_A, x_B) according to the current registrations):

$$\arg \min_{\alpha, \beta} \sum_{I_A \in I} \left(\sum_{I_B \in I \setminus I_A} \left(\sum_{(x_A, x_B) \in O_{AB}} (I_B(x_B) - [\alpha^{I_A} I_A(x_A) + \beta^{I_A}])^2 \right) \right) \quad (7)$$

Since this is equal to one-dimensional point correspondence registration, we can make use of the same iterative optimization algorithm used for image registration (4). To reduce influence of noise and computational costs, we use (precomputed) downsampled versions of the images for the optimization. A problem with unconstrained optimization is the possibility of convergence to the trivial solution of setting all pixel intensities to zero. We therefore formulate the linear transform $I(x) * \alpha + \beta$ as a weighted average between a linear transform, an additive transform and the identity transform:

$$\alpha I(x) + \beta = \lambda_1 * (\alpha' I(x) + \beta_1) + \lambda_2 * (I(x) + \beta_2) + \lambda_3 * I(x) \quad (8)$$

with user-definable regularization parameters $\lambda_1, \lambda_2, \lambda_3 : \lambda_1 + \lambda_2 + \lambda_3 = 1$. By using nonzero λ_2, λ_3 , we can constrain the optimization to not converge to the trivial solution.

The size of overlaps between image tiles can differ significantly. Therefore, intensity transformations supported by many overlapping pixels will implicitly have a higher weight, which can lead to the fact that visible intensity differences between tiles with little overlap persist. To compensate this effect we allow to balance overlaps by setting a maximal number of corresponding pixels. To ensure equal distribution of these corresponding pixels, we randomly remove pixels from the set of all pixels until the desired number is achieved.

8. Expansion Microscopy Protocol

Acryloyl-X, SE (6-((acryloyl)amino)hexanoic acid, succinimidyl ester; here abbreviated AcX; Thermo-Fisher) was resuspended in anhydrous DMSO at a concentration of 10 mg/mL, aliquoted and stored frozen in a desiccated environment. AcX stock solution was diluted in 1xPBS to a final concentration of 0.1 mg/mL AcX. Specimens were incubated in this 0.1mg/mL AcX solution for > 6 h, at RT. Monomer solution (1xPBS, 1M NaCl, 1.84M sodium acrylate, 0.35M acrylamide, 3.2mM N,N'-methylenebisacrylamide) was mixed, frozen in aliquots, thawed fully, vortexed, and cooled to 4°C before use. Concentrated stocks of the initiator ammonium persulfate (APS, 10% w/w), accelerator tetramethylethylenediamine (TEMED, 10% v/w) and inhibitor 4-hydroxy-2,2,6,6-tetramethylpiperidin-1-oxyl (4-HT, 0.5% w/w) were prepared as concentrated stock solutions, which were frozen in aliquots and then fully thawed and vortexed before use. Initiator, accelerator and inhibitor stock solutions were added to the monomer solution at a ratio of 2uL each per 94uL monomer solution to produce complete monomer solution. Specimens were washed 2x15min in complete monomer solution, on ice with shaking. Specimens were transferred to 3D-printed gelation chambers sized 1cm x 1cm and 0.3mm deep, along with 30uL of complete monomer solution. Chamber was covered with a cover glass and transferred to a humidified 37°C incubator for 2hr for gelation and gel curing.

Proteinase K (New England Biolabs) was diluted 1:100 to 8 units/mL in digestion buffer (50 mM Tris (pH 8), 1 mM EDTA, 0.5% Triton X-100, 1 M NaCl) to produce proteinase solution. Gel was recovered from chamber and incubated fully immersed in proteinase solution overnight at RT, with shaking. The digested gel was next incubated in at least a 10-fold excess volume of monomer solution with accelerator and inhibitor (no initiator) 2x15min, followed by complete monomer solution 2x15min on ice, with shaking. (Initiator is omitted from the first two washes to prevent premature gelation.) During incubation, a glass slide and cover glass are coated with parafilm by laying parafilm with paper backing onto the glass surface (parafilm down) and scraping a razor blade across the backing, then removing the backing. A 5mL syringe filled with silicone grease was used to apply four dabs (approx. 50uL each) of grease to the glass slide, at the corners of a rectangle slightly smaller than the cover glass. The gel was transferred to the coated slide and excess fluid was removed. The cover glass was placed over the gel, parafilm side down, contacting the dabs of grease. The cover glass was gently pressed down, squeezing the grease, until the coverglass contacted and sat flat across the gel. Excess complete monomer solution was backfilled into the resulting chamber to impede access of atmospheric oxygen to the gel. The completed chamber was moved to the 37oC humidified incubator for 2hr for gelation and curing.

The resulting doubly-gelled specimen was recovered from the chamber, and excess gel was trimmed away. The trimmed double gel was washed in excess volumes of doubly deionized water for 0.25-2 h to expand. This step was repeated 3-5 times in fresh water, until the size of the expanding sample plateaued.

9. BigStitcher User Guide

The BigStitcher comes with extensive documentation that is hosted on the ImageJ wiki. The current version of the continuously updated user guide can be found at <https://imagej.net/BigStitcher#Documentation>.

10. Example Datasets for BigStitcher

We prepared three different examples of different size and complexity for testing the BigStitcher. We suggest to run BigStitcher on these first before applying it to your dataset. This allows you to quickly test features in an environment where you can easily ask for advice on GitHub or the ImageJ Forum.

The data can be downloaded from the Open Science Foundation <https://www.nature.com/sdata/policies/repositories>.

2d multi-tile dataset (2.8 MB)

Maximum intensity projection of the nervous system of a Drosophila larva containing 6 tiles and 3 channels each. You can download the raw input at http://preibischlab.mdc-berlin.de/BigStitcher/Grid_2d.zip and a reconstructed BigStitcher project at http://preibischlab.mdc-berlin.de/BigStitcher/Grid_2d_h5_aligned.zip. In the reconstructed project, the images were imported into the BigStitcher using the AutoLoader (with immediate resaving as HDF5 and Movement to a regular 2-by-3 grid with 10% overlap between the tiles). We calculated pairwise shifts using phase correlation with default parameters, using the precomputed 2x2 downsampling and averaging the channels. We ignored links with correlation < 0.7 and calculated the final registration using the two-round global optimization with strict constraints.

3d multi-tile dataset (123 MB)

3d confocal scan of the nervous system of a Drosophila larva containing 6 tiles and 3 channels each, channels are distributed over different files. You can download the raw input at http://preibischlab.mdc-berlin.de/BigStitcher/Grid_3d.zip and the reconstructed project at http://preibischlab.mdc-berlin.de/BigStitcher/Grid_3d_h5_aligned.zip. In the reconstructed project, we ran the same import and reconstruction steps as for the 2d dataset and in addition performed affine refinement of the registration using IPC with default parameters and simple tile refinement to create the final reconstructed project.

We will add larger and more complex examples on the BigStitcher website <https://imagej.net/BigStitcher> and will also link videos of the alignment process from there.

11. Links to the current source codes

The BigStitcher is distributed over two projects. Both are licensed under the GPL(v2) and the source code is freely available on GitHub, at <https://github.com/PreibischLab/BigStitcher> and <https://github.com/PreibischLab/multiview-reconstruction>, respectively.

The CUDA code for accelerated interest point detection and devonvolution is available from <https://github.com/StephanPreibisch/SeparableConvolutionCUDALib> and <https://github.com/StephanPreibisch/FourierConvolutionCUDALib>, respectively.

Newer versions will be hosted using GitHub, and release announcements will be done via Twitter (<https://twitter.com/preibischs>), on the GitHub page (<https://github.com/PreibischLab/BigStitcher>), and on the ImageJ wiki (<https://imagej.net/BigStitcher>). Releases are and will be provided to end users via the Fiji update mechanism.¹⁵

REFERENCES

- [1] Arganda-Carreras, I., Kaynig, V., Rueden, C., Eliceiri, K. W., Schindelin, J., Cardona, A., and Sebastian Seung, H., “Trainable Weka Segmentation: a machine learning tool for microscopy pixel classification,” *Bioinformatics* **33**(15), 2424–2426 (2017).
- [2] Pietzsch, T., Saalfeld, S., Preibisch, S., and Tomancak, P., “BigDataViewer: visualization and processing for large image data sets,” *Nature methods* **12**(6), 481 (2015).

- [3] Pietzsch, T., Preibisch, S., Tomančák, P., and Saalfeld, S., “ImgLib2—generic image processing in Java,” *Bioinformatics* **28**(22), 3009–3011 (2012).
- [4] Linkert, M., Rueden, C. T., Allan, C., Burel, J.-M., Moore, W., Patterson, A., Loranger, B., Moore, J., Neves, C., MacDonald, D., et al., “Metadata matters: access to image data in the real world,” *The Journal of cell biology* **189**(5), 777–782 (2010).
- [5] Preibisch, S., Saalfeld, S., and Tomancak, P., “Globally optimal stitching of tiled 3D microscopic image acquisitions,” *Bioinformatics* **25**(11), 1463–1465 (2009).
- [6] Kuglin, C., “The phase correlation image alignment method,” in [Proc. IEEE International Conference on Cybernetics and Society, 1975], (1975).
- [7] Baker, S. and Matthews, I., “Lucas-Kanade 20 years on: A unifying framework,” *International journal of computer vision* **56**(3), 221–255 (2004).
- [8] Lowe, D. G., “Distinctive image features from scale-invariant keypoints,” *International journal of computer vision* **60**(2), 91–110 (2004).
- [9] Preibisch, S., Saalfeld, S., Schindelin, J., and Tomancak, P., “Software for bead-based registration of selective plane illumination microscopy data,” *Nature methods* **7**(6), 418 (2010).
- [10] Smith, C. S., Preibisch, S., Joseph, A., Abrahamsson, S., Rieger, B., Myers, E., Singer, R. H., and Grunwald, D., “Nuclear accessibility of β -actin mRNA is measured by 3D single-molecule real-time tracking,” *J Cell Biol* **209**(4), 609–619 (2015).
- [11] Fischler, M. A. and Bolles, R. C., “Random sample consensus: a paradigm for model fitting with applications to image analysis and automated cartography,” in [Readings in computer vision], 726–740, Elsevier (1987).
- [12] Saalfeld, S., Cardona, A., Hartenstein, V., and Tomančák, P., “As-rigid-as-possible mosaicking and serial section registration of large ssTEM datasets,” *Bioinformatics* **26**(12), i57–i63 (2010).
- [13] Saalfeld, S., Fetter, R., Cardona, A., and Tomancak, P., “Elastic volume reconstruction from series of ultra-thin microscopy sections,” *Nature methods* **9**(7), 717 (2012).
- [14] Blasse, C., Saalfeld, S., Etournay, R., Sagner, A., Eaton, S., and Myers, E. W., “PreMosa: extracting 2D surfaces from 3D microscopy mosaics,” *Bioinformatics* **33**(16), 2563–2569 (2017).
- [15] Schindelin, J., Arganda-Carreras, I., Frise, E., Kaynig, V., Longair, M., Pietzsch, T., Preibisch, S., Rueden, C., Saalfeld, S., Schmid, B., et al., “Fiji: an open-source platform for biological-image analysis,” *Nature methods* **9**(7), 676 (2012).